RESEARCH ARTICLE

NANO · MICRO small
www.small-journal.com

A Self-Cascade Oxygen-Generating Nanomedicine for Multimodal Tumor Therapy

*Jingyuan Zhao, Qi Sun, Dongze Mo, Jiayuan Feng, Yuting Wang, Tong Li, Yihong Zhang, and Hui Wei**

Natural and artificial enzyme oxygen-generating systems for photodynamic therapy (PDT) are developed for tumor treatment, yet they have fallen short of the desired efficacy. Moreover, both the enzymes and photosensitizers usually need carriers for efficient delivery to tumor sites. Here, a self-cascade-enhanced multimodal tumor therapy is developed by ingeniously integrating self-cascade-enhanced PDT with Zn^{2+}-overloading therapy. Manganese-porphyrin (TCPP-Mn) is chosen both as the photosensitizer and catalase (CAT) mimic, which can be encapsulated within glucose oxidase (GOx). Acid-responsive zeolitic imidazolate framework-8 (ZIF-8) is applied as the carrier for TCPP-Mn@GOx (T@G), attaining TCPP-Mn@GOx@ZIF-8 (T@G@Z). T@G@Z demonstrates robust anti-tumor ability as follows: upon the structural degradation of ZIF-8, GOx can mediate the oxidation of glucose and generate hydrogen peroxide (H_2O_2); TCPP-Mn can catalyze H_2O_2 into O_2 for self-cascade-enhanced PDT; meanwhile, the released Zn^{2+} can enhance oxidative stress and induce mitochondrial dysfunction by destroying mitochondrial membrane potential; furthermore, immunotherapy can be activated to resist primary tumor and tumor metastasis. The self-cascade-enhanced T@G@Z exhibited its potential application for further tumor management.

1. Introduction

Photodynamic therapy (PDT), as a burgeoning strategy for tumor management, involves photosensitizer-mediated light irradiation, converting oxygen molecules into cytotoxic reactive oxygen species (ROS) (i.e., singlet oxygen).[1] The PDT process consumes oxygen, and its efficacy can be limited by the hypoxic tumor microenvironment (TME), owing to the further elevated tumor hypoxia and possible adverse effects, such as tumor invasion and metastasis.[2] Hence, strategies have been explored to relieve the hypoxic TME, such as the involvement of oxygen carriers (hemoglobin[3] and perfluorocarbon)[4] and the usage of reactive oxygen supply materials (MnO_2[5] and gold nanoclusters).[6] Moreover, natural and artificial enzymes have been combined to generate O_2 through cascade reactions.[7] Considering the inadequate intratumoral H_2O_2 levels (5×10^{-5} to 1×10^{-4} M) to mediate H_2O_2-related therapies, extra generation of H_2O_2 is an aid.[8] Glucose oxidase (GOx), a starvation therapy inducer,[9] can catalyze intracellular glucose to generate H_2O_2, contributing to the combination of starvation therapy and other treatments (e.g., chemotherapy).[10] A two-enzyme nanoparticle, GOx-Mn/hyaluronic acid, was reported, where GOx can catalyze the conversion of glucose to gluconic acid and generate H_2O_2; furthermore, H_2O_2 is decomposed into O_2 due to its catalase (CAT)-like ability.[11] A dual enzyme-based nanostructure consisting of GOx and PdMo nanozyme was reported, where GOx can produce H_2O_2, which can be decomposed by PdMo nanozyme into cytotoxic hydroxyl radicals due to its peroxidase-like activity in acidic environments.[12]

Zeolitic imidazolate framework-8 (ZIF-8) has long been employed as a drug delivery carrier in various biomedical areas, exhibiting acid-responsive drug release capacity.[13] Zinc ions can be released from ZIF-8 in acidic environments. They are the second most abundant transition metal ion involved in multifarious cell activities, including cell survival, cell proliferation, and cell apoptosis.[14] In addition, zinc ions may also be associated with cancer initiation and progression.[15] Intracellular zinc homeostasis plays an important role in cell signal transduction, the disturbance of which will cause various cell responses and even cell apoptosis.[16] Superfluous Zn^{2+} can irreversibly block energy production via NAD^+ loss and inhibition of glycolysis.[17] Excessive Zn^{2+} can inhibit the mitochondrial electron transfer chain, causing the explosion of mitochondrial ROS.[18] Studies reported that Zn^{2+} overload can cause pyroptosis via a caspase-1/gasdermin D (GSDMD)-dependent pathway[19] and enhance the cGAS/STING signals.[20] In addition, it can increase cell susceptibility to

J. Zhao, Q. Sun, D. Mo, J. Feng, Y. Wang, T. Li, Y. Zhang, H. Wei
College of Engineering and Applied Sciences
Nanjing National Laboratory of Microstructures
Jiangsu Key Laboratory of Artificial Functional Materials
Nanjing University
Nanjing, Jiangsu 210023, China
E-mail: weihui@nju.edu.cn
H. Wei
State Key Laboratory of Analytical Chemistry for Life Science
School of Chemistry and Chemical Engineering
Chemistry and Biomedicine Innovation Center (ChemBIC)
Nanjing University
Nanjing, Jiangsu 210023, China

The ORCID identification number(s) for the author(s) of this article can be found under https://doi.org/10.1002/smll.202403523

DOI: 10.1002/smll.202403523

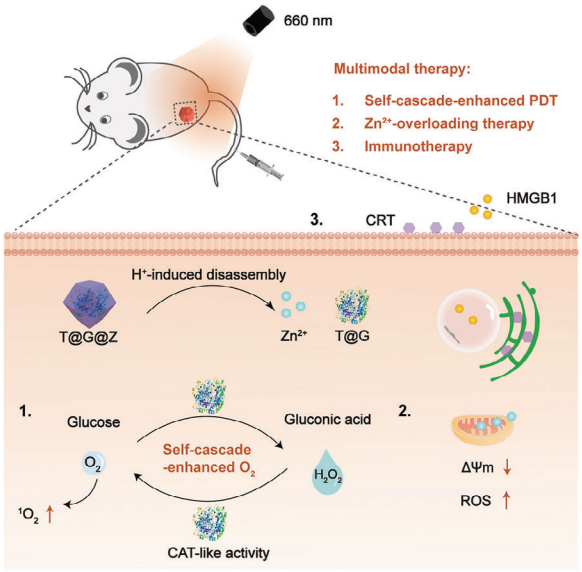

Figure 1. Mechanisms of T@G@Z for self-cascade-enhanced multimodal tumor therapies. 1) Self-cascade-enhanced photodynamic therapy via self-cascade-produced O_2; 2) Zn^{2+}-overloading therapy owing to Zn^{2+} released after structural degradation of ZIF-8 in the acidic tumor microenvironment; 3) Immunotherapy arising from photodynamic therapy and Zn^{2+}-overloading therapy.

apoptosis, enabling zinc supplementation as an unusual option for cancer management.[21] Nonetheless, sole administration of zinc ions fails to evoke robust death of tumor cells in the complicated TME.[22] Therefore, zinc ion-based combination therapies may maximize anti-tumor efficacy via the utilization of strategies with synergetic mechanisms of action.

In this work, we synthesized a self-cascade-enhanced nanomedicine, TCPP-Mn@GOx@ZIF-8 (T@G@Z), where manganese-porphyrin (TCPP-Mn) was chosen both as the photosensitizer and catalase mimic. TCPP-Mn was encapsulated within GOx, obtaining TCPP-Mn@GOx (T@G). Furthermore, ZIF-8 was adopted as the carrier for T@G, attaining T@G@Z. As shown in **Figure 1**, upon the structural degradation of the carrier ZIF-8 in the acidic tumor microenvironment, T@G was released. GOx mediated the oxidation of glucose and generated H_2O_2, which was further decomposed into oxygen by TCPP-Mn due to its CAT-like ability. On the one hand, the generated oxygen potentiated the catalytic process of GOx. On the other hand, upon light irradiation (660 nm), the singlet oxygen produced effectively killed tumor cells, achieving PDT. Moreover, Zn^{2+} release led to incremental intracellular ROS levels and loss of mitochondrial membrane potential, mediating Zn^{2+}-overloading therapy. Furthermore, immunotherapy could be activated to resist primary tumor and tumor metastasis,[23] demonstrating the potential to efficiently ablate tumors.

2. Results and Discussion

2.1. Synthesis and Characterization of T@G@Z

T@G@Z was a ZIF-8-based core-shell nanoparticle, where ZIF-8 acted as the carrier to encapsulate the cargo, T@G. T@G@Z was synthesized according to the strategy shown in **Figure 2a**. Briefly, considering the toxicity and hydrophobicity of TCPP-Mn and the hydrophobic region in the structure of GOx, we hypothesized that TCPP-Mn could be encapsulated within GOx (Figure S1, Supporting Information). Nevertheless, the exact interaction between TCPP-Mn and GOx remains to be studied. Then, T@G was encapsulated in ZIF-8, forming a core-shell MOF structure via a biomineral strategy. Particularly, the proteinous GOx played the role of a surfactant and enhanced the growth of crystal nuclei during the MOF formation.[24] As shown in Figure 2b,c and Figure S2 (Supporting Information), sole ZIF-8 had a regular dodecahedron structure, with a diameter of ≈ 100 nm. After encapsulation of GOx (G), TCPP-Mn (T), or T@G, the structure became irregular, with a slight increase in diameter (Figure S3, Supporting Information). The phenomenon was also confirmed by the results of dynamic light scattering (DLS) and zeta potential (Figure S4 and Table S1, Supporting Information). The conspicuous change of zeta potential from positive to negative demonstrated the formation of T@G@Z. As shown in Figure 2f, X-ray diffraction (XRD) patterns demonstrated the successful synthesis of ZIF-8 nanoparticles and the subsequent biomineralization had little impact on the structure of ZIF-8. In addition, the absorption spectra revealed the presence of TCPP-Mn in T@Z and T@G@Z, showing obvious absorption peaks (Figure 2d). SDS-PAGE analysis (Figure 2e) displayed the loading of GOx in G@Z and T@G@Z. The loading capacity of TCPP-Mn and GOx in T@G@Z was calculated to be 3.8% and 4.4%, respectively.

2.2. Functional Characterization and In Vitro PDT Efficacy of T@G@Z

With T@G@Z in hand, we further measured its properties and the efficacy of PDT under NIR light (660 nm) in vitro. First, the biostability of ZIF-8, G@Z, T@Z, and T@G@Z was evaluated by dispersing the four types of nanoparticles in water, DMEM (containing 10% FBS), and phosphate buffer (pH 5.7 and 6.3) for one week. As shown in Figure S5 (Supporting Information), all four types of nanoparticles exhibited good biostability in water and DMEM (containing 10% FBS) within one week, without significant vibration in size. In contrast, when dispersed in phosphate buffer (pH 5.7), the structure of ZIF-8-based nanoparticles became unstable within 3 days, displaying acid-responsive capacity (Figure S6, Supporting Information). The trend in the change of the size of the nanoparticles dispersed in the phosphate buffer (pH 6.3) was similar to that in the phosphate buffer (pH 5.7) (Figure S7). Furthermore, the catalytic activity of GOx and TCPP-Mn was characterized using a dissolved oxygen meter. Figure S8 (Supporting Information) and Figure 2g respectively showed the catalytic activity of GOx encapsulated in ZIF-8 before and after pretreatment with phosphate buffer (pH 5.7) for 24 h, by measuring the change in dissolved oxygen within 10 min with glucose as the substrate. In Figure S8 (Supporting Information), an inconspicuous change was observed in the dissolved oxygen. Nonetheless, after the collapse of the ZIF-8 shell, the value of dissolved oxygen remarkably declined in the G@Z group, demonstrating good catalytic activity of GOx. In the T@G@Z group, the value of dissolved oxygen was reduced in a more tempered way

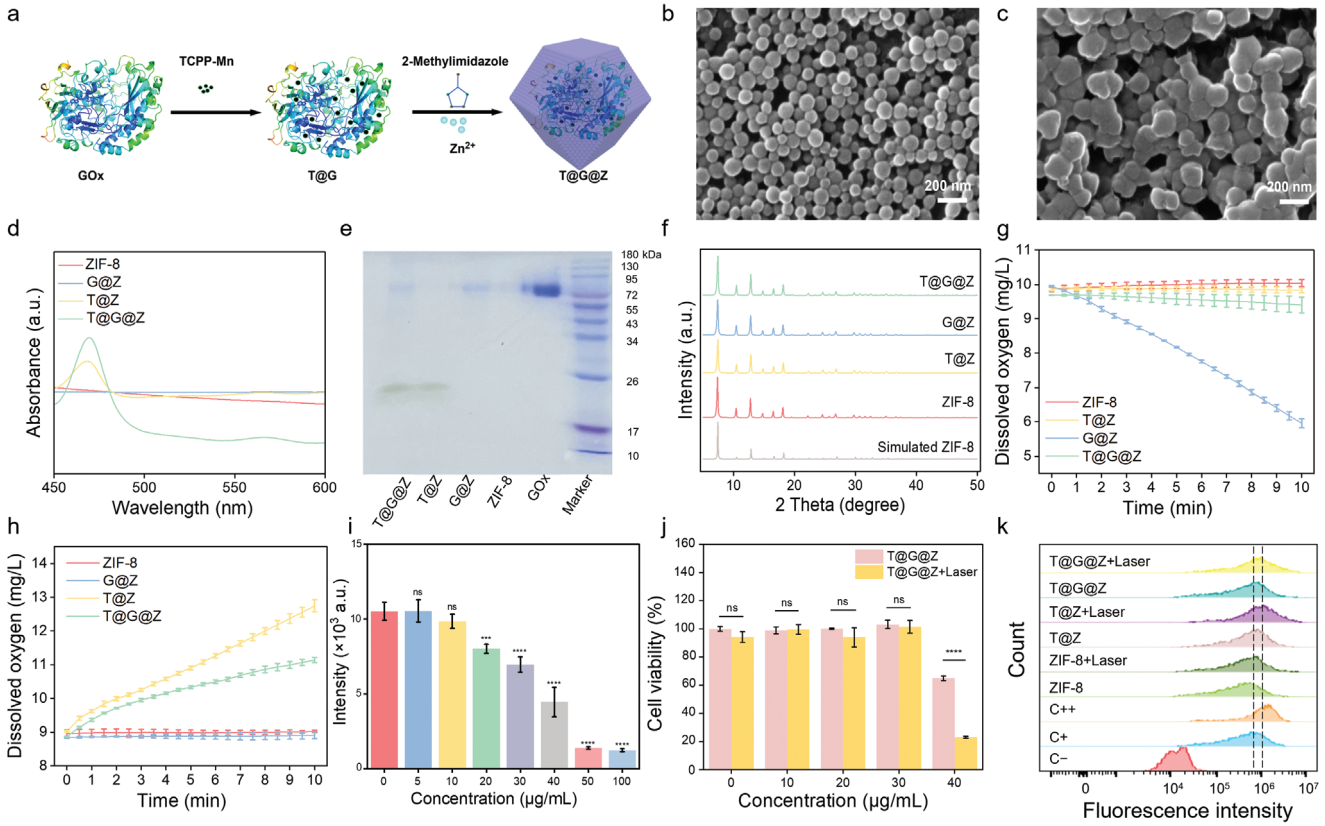

Figure 2. Preparation, characterization, and functional evaluation of T@G@Z. a) Schematic illustration of the synthesis of T@G@Z via a biomineralization strategy. SEM images of b) ZIF-8 and c) T@G@Z. d) Absorption spectra of ZIF-8, G@Z, T@Z, and T@G@Z. e) SDS-PAGE analysis of ZIF-8, G@Z, T@Z, and T@G@Z. f) XRD patterns of ZIF-8, G@Z, T@Z, and T@G@Z. g) The concentration of dissolved oxygen after the pretreatment in phosphate buffer (pH 5.7) within 10 min with glucose (8.3 mM) as the substrate (Data are shown as mean ± SD, n = 3). h) Time-dependent oxygen generation within 10 min with H_2O_2 (8.3 mM) as the substrate (Data are shown as mean ± SD, n = 3). i) Concentration-dependent singlet oxygen produced by T@G@Z under 660 nm laser irradiation (Data are shown as mean ± SD, n = 3, *** refers to $p < 0.001$, **** refers to $p < 0.0001$, ns refers to no significance, 0 μg mL^{-1} group served as the control for significance analysis). j) In vitro PDT efficacy of T@G@Z in 4T1 cells (Data are shown as mean ± SD, n = 3, **** refers to $p < 0.0001$, ns refers to no significance). k) Quantification of intracellular ROS in 4T1 cells under 660 nm laser irradiation detected by flow cytometry. C− group: 4T1 cells; C+ group: 4T1 cells + DCFH-DA probe; C++ group: 4T1 cells + DCFH-DA probe + H_2O_2.

compared with the G@Z group, mainly due to GOx consuming oxygen as well as generating H_2O_2. The produced H_2O_2 is decomposed into oxygen by TCPP-Mn due to its catalase-like activity, achieving the self-cascade-enhanced O_2 supply (Figure 2g). However, the tumor microenvironment exhibited a high concentration of H_2O_2. Therefore, we hypothesized that T@G@Z would provide sufficient oxygen for PDT. Figure 2h shows the catalytic activity of TCPP-Mn encapsulated in ZIF-8 by measuring the change in dissolved oxygen within 10 min, using H_2O_2 as the substrate. The catalytic activity of T@Z was slightly better than T@G@Z, owing to the loss of TCPP-Mn in T@G in the dialysis process.

The above studies confirmed the catalytic activity of GOx and TCPP-Mn encapsulated in the ZIF-8 shell. We further identified the production of singlet oxygen under NIR light (660 nm, 1 W cm^{-2}, 5 min) with ABDA probe (Figure 2i) and SOSG probe (Figure S9, Supporting Information). When ABDA reacts with singlet oxygen, it will be photobleached. Therefore, the fluorescence intensity will decrease (Figure S10, Supporting Information). Before SOSG reacts with singlet oxygen, the fluorescence will quench because of internal electron transfer. After SOSG reacts with singlet oxygen, SOSG endoperoxide will form. In that case, internal electron transfer is inhibited, and green fluorescence will be observed (Figure S11, Supporting Information). When the concentration of T@G@Z was 50 μg mL^{-1}, singlet oxygen production was remarkable. The electron spin resonance (ESR) experiment was also performed to detect the singlet oxygen. Under NIR light (660 nm, 1 W cm^{-2}, 5 min), T@G@Z can produce singlet oxygen (Figure S12, Supporting Information). Notably, ZIF-8 could intrinsically cause apoptosis of 4T1 cells in a concentration-dependent manner (Figure S13, Supporting Information) while PDT aggravated this phenomenon (Figure S14, Supporting Information). At the cellular level, ≈ 80% of 4T1 cells were killed in the T@G@Z+Laser group at the concentration of 40 μg mL^{-1} (Figure 2j). Furthermore, overall ROS production within 4T1 cells with and without PDT was measured via flow cytometry, where the positive control group was pretreated with 2.5 mM H_2O_2 for 1 h (Figure S15, Supporting Information). Figure 2k presented that PDT enhanced overall ROS production in 4T1 cells (Figures S16 and S17, Supporting Information).

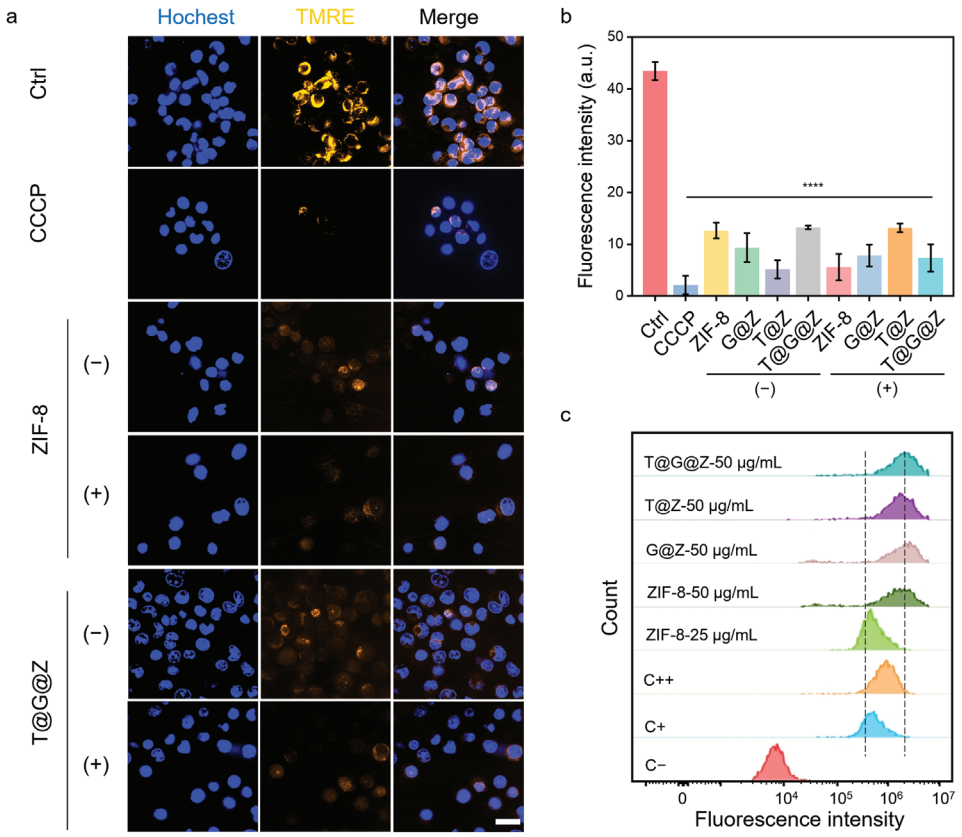

Figure 3. ROS production and loss of mitochondrial membrane potential caused by T@G@Z. a) Confocal fluorescence images showing the mitochondrial membrane potentials of 4T1 cells. Scale bar: 25 μm. (−): without a 660 nm laser; (+): with a 660 nm laser. b) Quantitative analysis of fluorescence intensity in (a) and Figure S18 (Supporting Information) (Data are shown as mean ± SD, n = 3, **** refers to $p < 0.0001$, Ctrl group served as the control for significance analysis). c) Quantification of intracellular ROS in 4T1 cells pretreated by different groups detected by flow cytometry. C− group: 4T1 cells; C+ group: 4T1 cells + DCFH-DA probe; C++ group: 4T1 cells + DCFH-DA probe + H_2O_2.

2.3. T@G@Z Augmented ROS Level and Destroyed Mitochondrial Membrane Potential

In the above studies, the phenomenon that ZIF-8-based nanoparticles could intrinsically cause the apoptosis of 4T1 cells aroused our interest. Upon reviewing the mechanism of the ZIF-8-based nanoparticles, we meticulously attributed it to zinc ions released upon degradation of ZIF-8, as the 2-methylimidazole ligand was reported to be nontoxic even at a high concentration of 100 μg mL^{-1}.[25] Zinc is an essential trace metal in multitudinous biological activities, such as zinc-related catalytic reactions, DNA transcription, protein transport systems, stabilization of the membrane structure, and zinc-related signaling pathways.[26] Nonetheless, a balance of zinc should be strictly achieved, as either deficiency or overload will induce augmented cellular oxidative stress. Therefore, the intracellular ROS induced by ZIF-8-based nanoparticles was examined by flow cytometry. As shown in **Figure** 3c, after pretreatment with ZIF-8 for 8 h, no significant intracellular ROS increase was observed in 4T1 cells at a concentration of 25 μg mL^{-1}. In contrast, at a concentration of 50 μg mL^{-1}, an obvious enhancement in ROS level was observed, as well as other ZIF-8-based nanoparticles. In addition, zinc can interfere with the mitochondrial electron chain. Hence, we studied the change in mitochondrial membrane potential (ΔΨm) after treatment with ZIF-8-based nanoparticles. Figure 3a,b and Figure S18 (Supporting Information) presented that sole ZIF-8-based nanoparticles caused a remarkable loss of mitochondrial membrane potential in 4T1 cells, comparable to the CCCP-pretreated group. Meanwhile, no obvious variation was observed between the ZIF-8-based nanoparticles-pretreated groups with and without PDT, implying that the loss of mitochondrial membrane potential was owing to zinc ions.

2.4. In Vivo Anti-Tumor Efficacy of T@G@Z

The above studies have confirmed the killing effect of ZIF-8-based nanoparticles at the cellular level. Then, in vivo anti-tumor efficacy was studied in a subcutaneous 4T1 tumor-bearing model (**Figure** 4a). As the therapeutic nanoparticles were injected intravenously, the hemolytic phenomenon of ZIF-8-based nanoparticles was assessed. As shown in Figures S19 and S20 (Supporting Information), there was no hemolytic phenomenon in any of the nanoparticles and the hemolysis ratios were all below 5%. After treatment with ZIF-8-based nanoparticles, tumor size was reduced compared with the Ctrl group, mainly due to Zn^{2+}-overloading therapy mediated by Zn^{2+} released in the acidic tumor microenvironment. However, there was no

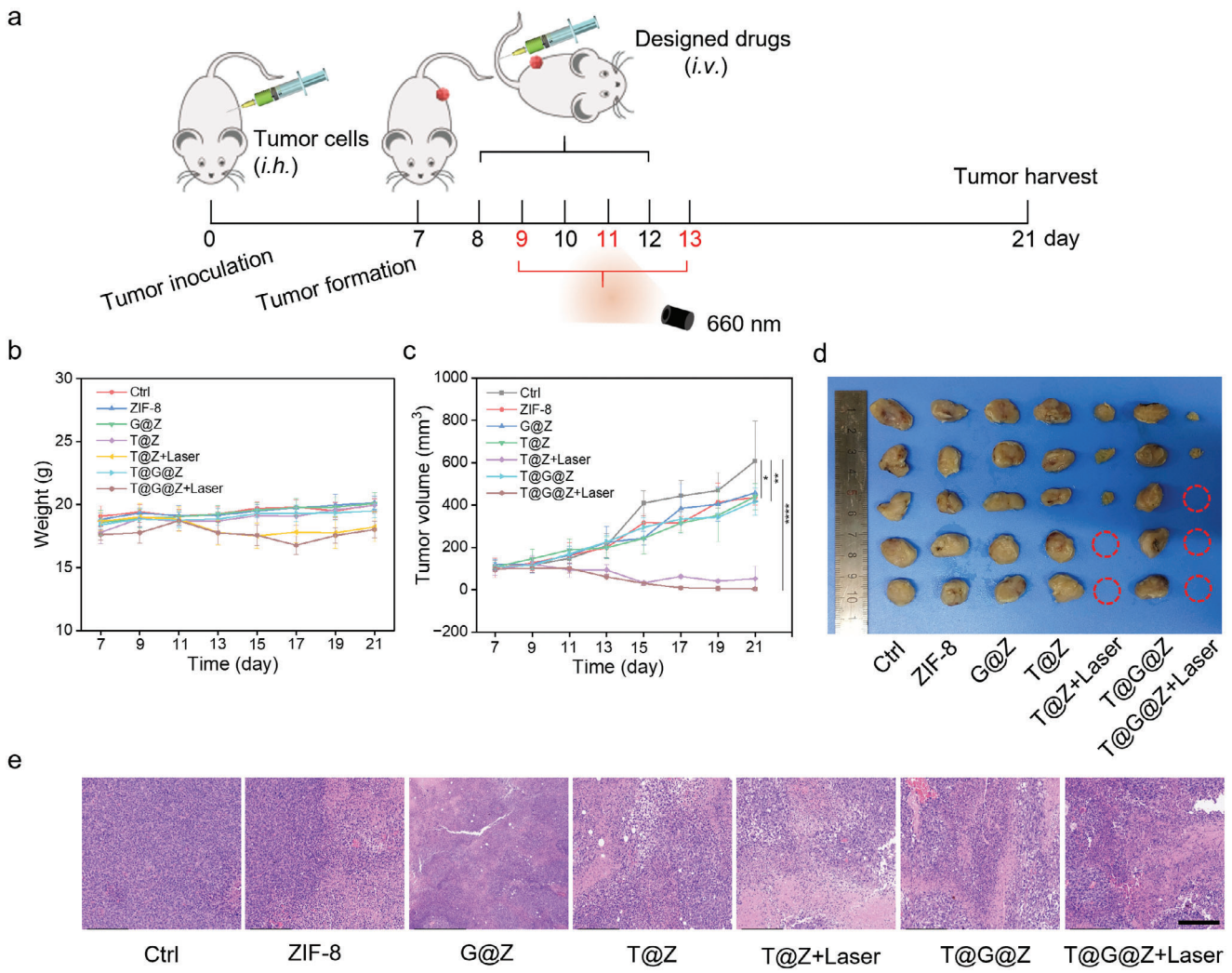

Figure 4. In vivo anti-tumor efficacy of T@G@Z. i.h. refers to hypodermic injection; i.v. refers to intravenous injection. a) Schematic illustration of the treatment regimen for BALB/c mice bearing 4T1 tumor. b) Time-dependent body weight change (Data are shown as mean ± SD, n = 5). c) Time-dependent tumor volume change (Data are shown as mean ± SD, n = 5, * refers to $p < 0.05$, ** refers to $p < 0.01$, **** refers to $p < 0.0001$). d) Photographs of the harvested tumors (n = 5). The red circle means that the tumor has disappeared. e) H&E staining results of the harvested tumors. Scale bar: 200 μm.

significant variance among the ZIF-8 group, G@Z group, T@Z group, and T@G@Z group. Tumor size in the T@Z+Laser group and T@G@Z+Laser group was significantly smaller than in other groups, with the T@G@Z+Laser group displaying the best anti-tumor capacity. In the T@Z+Laser group, the efficacy of PDT was limited due to insufficient oxygen in the tumor microenvironment (Figure 4c,d). Moreover, during the treatment period, no obvious weight change was observed in any of the treatment groups compared with the Ctrl group (Figure 4b). Furthermore, H&E staining results in Figure 4e displayed that, unlike the dense structure of the tumor tissue in the Ctrl group, the tumor structure of ZIF-8-based nanoparticles groups was damaged to different degrees after treatments.

The potential toxicity toward main organs was also investigated. H&E staining results in Figure S21 (Supporting Information) showed that there was minimal toxicity to major organs. We further dispersed T@G@Z nanoparticles in DMEM (containing 10% FBS) for 10 days, mimicking the environment in the blood full of proteins. We hypothesized a protein corona formed on the surface of nanoparticles would improve their biocompatibility, which was confirmed by the improved cell viability of 4T1 cells (Figure S22, Supporting Information).

2.5. T@G@Z Activated Anti-Tumor Immunity

We further studied the immunogenicity of 4T1 cells after treatment with different nanoparticles. High-mobility group box 1 (HMGB1) protein plays a significant role in mediating the local and systemic responses to cancer, and its release has important implications for cancer prevention and treatment.[27] Therefore, the release of HMGB1 from 4T1 cells after different treatments was measured via confocal laser scanning microscopy (CLSM). As shown in **Figures** 5a,c and S23 (Supporting Information), the

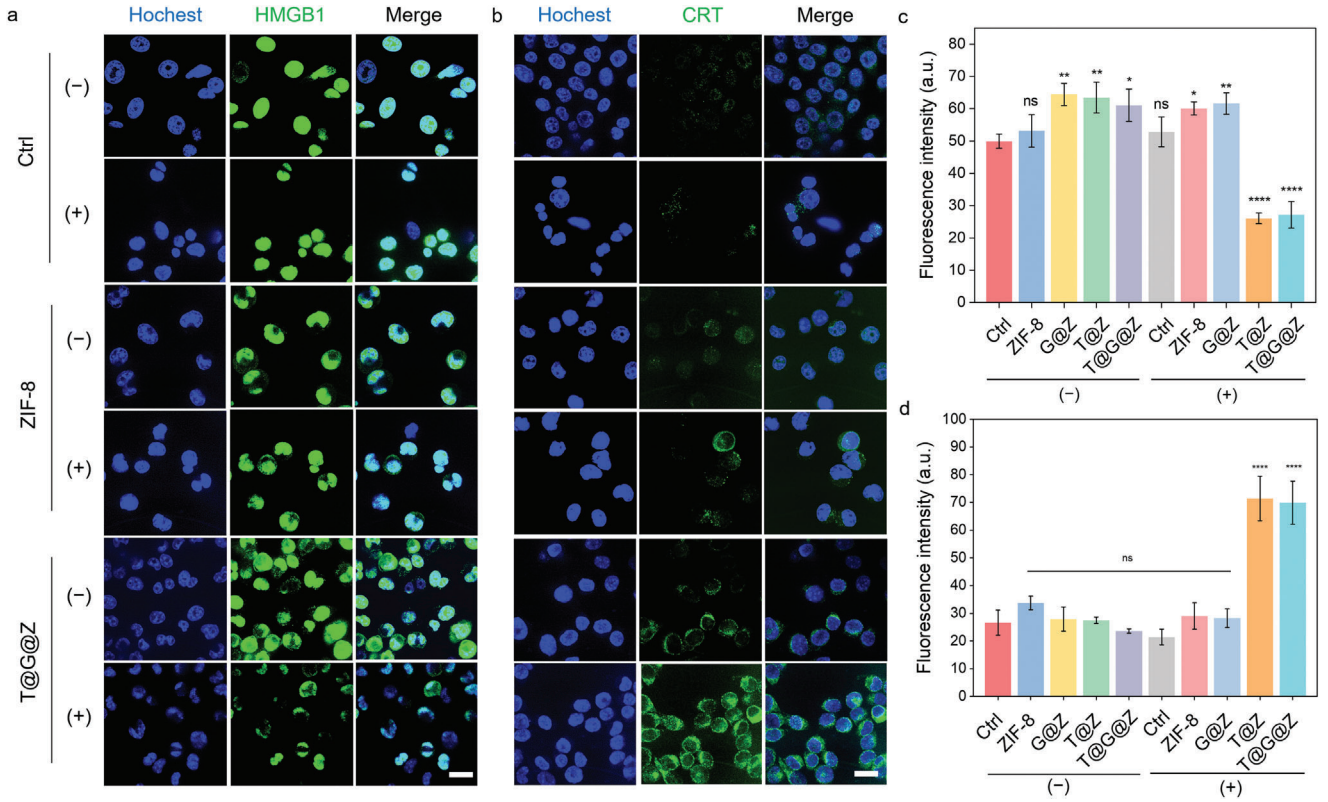

Figure 5. Release of HMGB1 and exposure of CRT. a) Confocal fluorescence images showing the expression of HMGB1 in 4T1 cells. Scale bar: 25 μm. (−): without a 660 nm laser; (+): with laser. b) Confocal fluorescence images showing the expression of CRT in 4T1 cells. Scale bar: 25 μm. (−): without a 660 nm laser; (+): with a 660 nm laser. c) Quantitative analysis of fluorescence intensity in (a) and Figure S23 (Supporting Information) (Data are shown as mean ± SD, n = 3, * refers to $p < 0.05$, ** refers to $p < 0.01$, **** refers to $p < 0.0001$, ns refers to no significance, Ctrl group served as the control for significance analysis). d) Quantitative analysis of fluorescence intensity in (b) and Figure S24 (Supporting Information) (Data are shown as mean ± SD, n = 3, **** refers to $p < 0.0001$, ns refers to no significance, Ctrl group served as the control for significance analysis).

HMGB1 level significantly declined in the T@Z+Laser group and T@G@Z+Laser group, mainly due to PDT.

Calreticulin (CRT), an endoplasmic reticulum (ER)-resident protein, takes part in various cellular processes.[28] Tumor cells that succumb to immunogenic cell death will expose CRT on their surface, further initiating anti-tumor immunity. Thus, we examined the CRT exposure on the surface of 4T1 cells after different treatments. Consistent with the release of HMGB1, the exposure of CRT was also evident in the T@Z+Laser group and T@G@Z+Laser group (Figure 5b,d; Figure S24, Supporting Information). Overall, the therapeutic nanoparticles had successfully activated anti-tumor immunity by the release of HMGB1 and exposure of CRT.

2.6. T@G@Z Achieved Anti-Metastasis

A mice lung anti-metastatic model was further established as shown in **Figure 6**a. After sacrificing the mice, their lungs were harvested and metastatic nodules were compared (Figure 6d,e). Compared with the Ctrl group, after treatment with different ZIF-8-based nanoparticles, metastatic nodules were fewer. Metastatic nodules in the T@Z+Laser group and the T@G@Z+Laser group were remarkably reduced, with the fewest metastatic nodules observed in the T@G@Z+Laser group, suggesting good anti-metastatic ability. During the treatment period, there was no significant variance in the weight of the mice (Figure 6b). The trend in tumor volume among the groups was similar to that in the subcutaneous 4T1 tumor-bearing model (Figure 6c). In addition, H&E staining results in Figure 6f showed that the structure of the lungs was destroyed obviously due to metastatic nodes in Ctrl group while in the ZIF-8 group, G@Z group, T@Z group, and T@G@Z group, the phenomenon was much better owing to fewer metastatic nodes. However, in the T@Z+Laser group and T@G@Z+Laser group, there were nearly no metastatic nodes, displaying fair anti-metastatic ability.

Although T@G@Z could accumulate at the tumor sites via the enhanced permeability and retention (EPR) effect and T@G@Z attained fair anti-tumor and anti-metastatic efficacy, more active targeting strategies can be adopted (e.g., hyaluronic acid,[29] folic acid,[30] and arginine-glycine-aspartic acid-cysteine[31]) for targeted drug delivery. In addition, various metals with anti-tumor biological effects (e.g., Mn^{2+}, Zn^{2+}, Cu^{2+}, and Fe^{2+}) have been studied for cancer therapy.[32] In this study, Mn^{2+} was used to mediate the catalytic reaction to decompose H_2O_2. Zn^{2+} overload was adopted to enhance oxidative stress and induce mitochondrial dysfunction. Nevertheless, precision medications targeting mitochondria can be further developed via modification

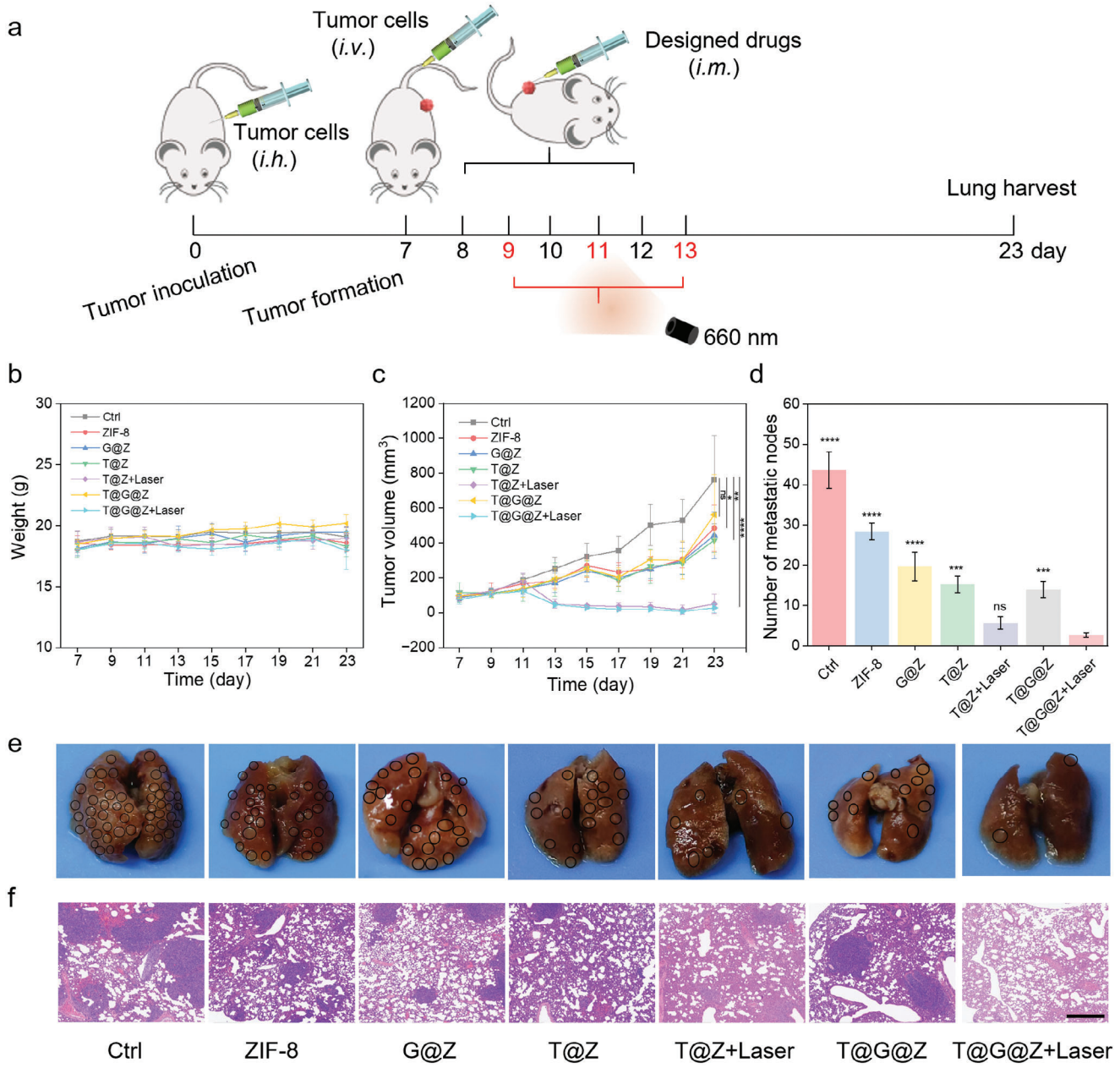

Figure 6. In vivo anti-metastatic efficacy of T@G@Z. i.h. refers to hypodermic injection; i.v. refers to intravenous injection; i.m. refers to intratumoral injection. a) Schematic illustration of establishment and treatment of the anti-metastatic model. b) Time-dependent body weight change (Data are shown as mean ± SD, n = 5). c) Time-dependent tumor volume change (Data are shown as mean ± SD, n = 5, * refers to $p < 0.05$, ** refers to $p < 0.01$, **** refers to $p < 0.0001$, ns refers to no significance). d) Statistic analysis of metastatic nodes (Data are shown as mean ± SD, n = 3, *** refers to $p < 0.001$, **** refers to $p < 0.0001$, ns refers to no significance). e) Photographs of the harvested lungs (Black circles are used to represent metastatic nodes). f) H&E staining results of the harvested lungs. Scale bar: 500 μm.

with functional groups (e.g., $-NH_2$, $-COOH$, and $-N_3$).[33] Traditional strategies of relieving hypoxia and delivering photosensitizers are multi-step and complicated where both the photosensitizer and the oxygen-generating materials need the carrier for efficient delivery.[34] To overcome this obstacle, TCPP-Mn serves both as the CAT mimic and the photosensitizer. Nevertheless, as for T@G@Z, the oxygen production depends on the decomposition of H_2O_2. For more effective hypoxic relief, both oxygen-generating and oxygen-delivering tactics can be adopted.

3. Conclusion

In summary, we designed and synthesized a self-cascade-enhanced nanomedicine, T@G@Z, via biomineralization. Considering the unique features of the tumor microenvironment

such as hypoxia, slight acidity, and high concentration of H_2O_2, self-cascade-enhanced PDT and Zn^{2+}-overloading therapy were combined to inhibit tumor growth and tumor metastasis. Due to Mn^{2+}, TCPP-Mn is a photosensitizer as well as a CAT mimic, which can not only produce singlet oxygen under NIR light (660 nm) but also form a cascade reaction with GOx, where the generated H_2O_2 is further decomposed into oxygen, alleviating the hypoxic microenvironment. The hydrophobicity and toxicity of TCPP-Mn made a proper delivery approach necessary. Considering the presence of the hydrophobic region in GOx, TCPP-Mn was encapsulated within GOx. ZIF-8 nanoparticles have been frequently employed as drug carriers, mainly attributed to their acid-responsive ability. After structural degradation in the acidic environment, zinc ions and the cargo will be released. In this work, zinc ions were confirmed to augment the intracellular ROS level and induce mitochondrial dysfunction by destroying the mitochondrial membrane potential, mediating Zn^{2+}-overloading therapy. Further, the immunogenicity of tumor cells was successfully activated via the release of HMGB1 and the exposure of CRT, demonstrating its potential in tumor management.

4. Experimental Section

Chemicals and Reagents: All the reagents adopted were analytically pure without any additional treatment unless otherwise described. Zinc nitrate hexahydrate ($Zn(NO_3)_2{\cdot}6H_2O$), hydrogen peroxide, and ethanol were obtained from Sinopharm Chemical Reagent Co., Ltd. (Shanghai, China). 2-Methylimidazole was provided by Bide Pharmaceutical Technology Co., Ltd. (Shanghai, China). TCPP-Mn was provided by Chemsoon Co., Ltd. (Shanghai, China). Glucose oxidase (GOx, from *Aspergillus niger*) and dichlorofluorescein diacetate (DCFH-DA) were bought from Aladdin Biochemical Technology Co., Ltd. (Shanghai, China). The CCK-8 kit was from Dojindo Co., Ltd. (Shanghai, China). Reagents for cell culture include fetal bovine serum (from Excel Co., Ltd., Xi'an, China), HyClone DMEM (from Cytiva Co., Ltd., Shanghai, China), trypsin and penicillin-streptomycin (from Beyotime Co., Ltd., Shanghai, China) and Trypsin-EDTA Solution with phenol red (0.25% Trypsin) (from SenBeiJia Biological Technology Co., Ltd., Nanjing, China). 9,10-Anthracenediyl-bis(methylene)dimalonic acid (ABDA) was purchased from Shanghai MaoKang Biotechnology Co., Ltd. Singlet oxygen sensor green (SOSG) was from Meilunbio Co., Ltd. (Dalian, China). The SDS-PAGE kit was supplied by Beyotime Co., Ltd. (Shanghai, China). Glucose was purchased from Sigma-Aldrich Inc. (USA). Mitochondrial Membrane Potential Assay Kit with TMRE was from Beyotime Co., Ltd. (Shanghai, China). HMGB1 (Clone name: SA39-03, catalogue number: ET1601-2) and CRT (Clone name: SU37-03, catalogue number: ET1608-60) were from Shandong Huaan Biotechnology Co., Ltd. (Shandong, China). Hochest 33342 was from Thermo Fisher Scientific (USA). Hydrochloric acid was from Nanjing Chemical Reagent Co., Ltd. (Nanjing, China). 2,2,6,6-tetramethylpiperidine (TEMP) was from J&K Scientific Co., Ltd. (Beijing, China). The BCA protein assay kit was from Beijing Labgic Technology Co., Ltd. (Beijing, China).

Instrumentations: The morphology of the materials was measured with a Zeiss Ultra 55 scanning electron microscope (Germany) and a JEOL JEM-2800 electron transmission microscope (Japan). Size and zeta potential were measured with Malvern Zetasizer NanoZSP (UK). The X-ray diffraction (XRD) patterns of the materials were attained from a Bruker D8 advance X-ray diffractometer (Germany). The presence of TCPP-Mn was confirmed by a Shimadzu UV-3600 Plus UV–vis spectrophotometer (Japan). The change of the dissolved oxygen was studied with a Mettler Toledo dissolved oxygen meter (USA). Intracellular ROS level was studied with a Beckman Coulter CytoFLEX flow cytometer (USA). Confocal images were taken with an Olympus laser scanning confocal microscope (Japan). The structure of the protein was measured via an Applied Photophysics Chirascan circular dichroism spectrometer (UK). The 660 nm laser was from LEO Photonics Co., Ltd. (China). The content of metal elements in nanomaterials was measured via a PerkinElmer Avio 220 Max inductively coupled plasma optical emission spectrometry (USA). The ESR spectra were obtained from a Bruker EMX plus electron spin resonance spectrometer (Germany).

Preparation of T@G: Briefly, 750 µL of TCPP-Mn dissolved in DMSO solution (concentration: 1 mg mL^{-1}), 2250 µL of water, and 3 mL of GOx aqueous solution (concentration: 1 mg mL^{-1}) were stirred for 3 h in the dark and further dialyzed for 2 days in the dark, obtaining T@G.

Preparation of T@G@Z: T@G@Z was synthesized via a simple method. Briefly, 4 mL of 0.94 M 2-methylimidazole solution was first mixed with 6 mL of T@G solution for 5 min, and then 5 mL of 15 mM zinc nitrate hexahydrate solution was added. The whole reaction system was 15 mL and the reaction lasted 5 min, followed by a 30-min standing. In the reaction system, the final concentration of TCPP-Mn was 50 µg mL^{-1} and GOx was 0.2 mg mL^{-1}. After the reaction, T@G@Z was centrifuged and washed with deionized water for three times, and further freeze-dried for storage. The preparation of T@Z and G@Z was similar to the preparation of T@G@Z.

Stability of Materials: Different materials were dispersed in different buffers, such as water, DMEM (containing 10% FBS), and phosphate buffer (pH 5.7 and 6.3), for one week. During one week, every other day, the size of the materials was measured. At the end of one week, precipitates of the materials were collected to measure the morphology via SEM imaging.

Hemolysis Assay: The blood was extracted from BALB/c mice and washed with the PBS solution three times. Then, the blood solution was uniformly distributed into different groups of materials (n = 3). After the incubation for 1.5 h, the groups were centrifuged and the supernatant was collected and added to the 96-well plate. In the negative control, the PBS solution was adopted rather than the materials, while in the positive control, water was used. The absorbance value (Ab) at 540 nm was recorded via a microplate reader. Hemolysis ratios were calculated as follows:

$$\text{Hemolysis ratio} = \frac{\text{Ab (Experiments)} - \text{Ab (Negative)}}{\text{Ab (Positive)} - \text{Ab (Negative)}} \times 100\% \quad (1)$$

Change of the Dissolved Oxygen: The change of the dissolved oxygen during the oxidation of glucose was studied with a dissolved oxygen meter. When glucose was adopted as the substrate, the final concentration of glucose was 8.3 mM and the concentration of the materials was 660 µg mL^{-1}. The concentration of the dissolved oxygen was recorded every 30 s for 10 min. When hydrogen peroxide was adopted as the substrate, the final concentration of hydrogen peroxide was 8.3 mM and the concentration of the materials was 660 µg mL^{-1}. The concentration of the dissolved oxygen was recorded every 30 s for 10 min.

To study the acid-responsive ability of the materials, materials were pretreated with phosphate buffer (pH 5.7, 20 mM) for 24 h.

Production of Singlet Oxygen: Materials of different concentrations (0, 5, 10, 20, 30, 40, 50, and 100 µg mL^{-1}) were irradiated with a 660 nm laser (5 min, 1 W cm^{-2}). The working concentration of the two singlet oxygen probes ABDA and SOSG was referred to the instruction. The fluorescent intensity was measured via a microplate reader. As for the ABDA probe, λ_{ex} = 380 nm, λ_{em} = 407 nm. As for the SOSG probe, λ_{ex} = 504 nm, λ_{em} = 525 nm.

The electron spin resonance (ESR) experiment was also performed to study the singlet oxygen production. TEMP served as the singlet oxygen trapper. The working concentration of TEMP was 100 mM and the concentration of T@G@Z was 100 µg mL^{-1}. The solution was irradiated with a 660 nm laser (5 min, 1 W cm^{-2}).

Loading Capacity of TCPP-Mn and GOx in T@G@Z: The loading capacity of TCPP-Mn and GOx was calculated according to the following formula:

$$\text{Loading capacity} = \frac{\text{Weight of loaded TCPP} - \text{Mn or GOx in the nanoparticle}}{\text{Weight of the nanoparticle}} \times 100\% \quad (2)$$

As for the loading capacity of TCPP-Mn, Mn content in the nanoparticles was detected via an ICP-OES. Then, TCPP-Mn content was further calculated.

As for the loading capacity of GOx, T@G@Z was treated with diluted hydrochloric acid for 24 h to release GOx and then the BCA assay was adopted.

Photodynamic Efficacy of Materials at the Cellular Level: 4T1 cells were used in the experiment. First, 4T1 cells were refreshed and further cultured in high glucose-DMEM (10% FBS) in an incubator (37 °C, 5% CO_2). Then, the cells were sub-cultured in a 96-well plate with a seeding density of 8×10^3 cells per well for 12 h.

Then, the cells were refreshed with a culture medium containing materials of different concentrations for 4 h, followed by irradiation with a 660 nm laser (10 min, 1 W cm^{-2}). Subsequently, the CCK-8 kit was used to assess the cell viability, and the absorbance value at 450 nm was recorded. Additionally, the 12-hour cell viability of different materials at different concentrations was measured for comparison.

Measurement of Intracellular ROS Level via the Flow Cytometer: 4T1 cells were used in the experiment. First, 4T1 cells were refreshed and further cultured in high glucose-DMEM (10% FBS) in an incubator (37 °C, 5% CO_2). Then, the cells were subcultured in a 6-well plate for 12 h.

For the measurement of ROS induced by zinc ions, the cells were refreshed with the culture medium containing different materials at two concentrations (25 and 50 μg mL^{-1}) and further incubated for 8 h. Incubation time was meticulously chosen to avoid the apoptosis of the cells. Then, the cells were collected and incubated with a DCFH-DA probe for 30 min, followed by measurement using a flow cytometer.

For the measurement of ROS induced by PDT, the cells were refreshed with the culture medium containing different materials at the concentration of 50 μg mL^{-1} and further incubated for 4 h, followed by irradiation with a 660 nm laser (10 min, 1 W cm^{-2}). The total incubation time was 6 h. Then, the cells were collected and incubated with a DCFH-DA probe for 30 min, followed by measurement with a flow cytometer.

Measurement of Intracellular ROS Level via a Laser Scanning Confocal Microscope: 4T1 cells were used in the experiment. First, 4T1 cells were refreshed and further cultured in high glucose-DMEM (10% FBS) in an incubator (37 °C, 5% CO_2). Then, the cells were subcultured in a 6-well plate for 12 h. Subsequently, the cells were refreshed with the culture medium containing different materials at the concentration of 50 μg mL^{-1} and further incubated for 4 h, followed by irradiation with a 660 nm laser (10 min, 1 W cm^{-2}). The total incubation time was 8 h. Then, the cells were washed with PBS and further incubated with Hochest 33342 and DCFH-DA for 30 min, followed by measurement with a laser scanning confocal microscope.

Measurement of Mitochondrial Membrane Potential: 4T1 cells were used in the experiment. First, 4T1 cells were refreshed and further cultured in high glucose-DMEM (10% FBS) in an incubator (37 °C, 5% CO_2). Then, the cells were subcultured in a 6-well plate for 12 h. Subsequently, the cells were refreshed with the culture medium containing different materials at the concentration of 50 μg mL^{-1} and further incubated for 4 h, followed by irradiation with a 660 nm laser (10 min, 1 W cm^{-2}). The total incubation time was 8 h. Then, the cells were washed with PBS and further incubated with Hochest 33342 and mitochondrial Membrane Potential Assay Kit with TMRE for 30 min, followed by measurement with a laser scanning confocal microscope.

Immunofluorescence Analysis of 4T1 Cells: 4T1 cells were used in the experiment. First, 4T1 cells were refreshed and further cultured in high glucose-DMEM (10% FBS) in an incubator (37 °C, 5% CO^2). Then, the cells were subcultured in a 6-well plate for 12 h. Subsequently, the cells were refreshed with the culture medium containing different materials at the concentration of 50 μg mL^{-1} and further incubated for 4 h, followed by irradiation with a 660 nm laser (10 min, 1 W cm^{-2}). Calreticulin (CRT) and high mobility group protein 1 (HMGB1) antibodies were used in the experiment and further measured via a laser scanning confocal microscope.

Anti-Tumor Efficacy Analysis: Female BALB/c mice (6-8 weeks old) were purchased from Beijing Vital River Laboratory Animal Technology Co., Ltd. All animal experiments were approved by the Institutional Animal Care and Use Committee (IACUC) of Nanjing University (IACUC-2212004). The anti-tumor model was established as follows: 4T1 cells were cultured, collected, and washed with PBS several times. Subsequently, 4T1 cells were dispersed in PBS solution and subcutaneously injected into the right flank of mice (density: 1×10^6 cells per mouse). The volume of tumors was monitored and calculated according to the formula V = length × $width^2$ / 2. The length and width of the tumors were measured with a digital caliper. Once the tumor volume reached ≈100 mm^3, the mice were grouped according to the experimental plan and injected with different materials intravenously (5 mg kg^{-1} per mouse). For groups requiring irradiation, 12 h after the injection of the materials, the tumors were irradiated with a 660 nm laser for 5 min at 1 W cm^{-2}. During the treatments, the size of the tumors was monitored. After the whole treatment, the mice were further kept for several days. Finally, tumors were harvested. The major organs, such as the heart, liver, spleen, lung, and kidney, were also harvested for biosafety assessment.

Anti-Metastatic Efficacy Analysis: The establishment of the anti-metastatic model was similar to the anti-tumor model. After the tumor formation, a suspension of 4T1 cells was intravenously injected into the mice. Subsequently, the mice were treated according to the plan mentioned above. The difference is that the materials were administered via intratumor injection. After the whole treatment process, the lungs were harvested for anti-metastatic efficacy analysis. The metastatic nodes were calculated and the lungs were further subjected to an H&E staining assay.

Statistical Analysis: Statistical tests were performed using GraphPad Prism (Version 9.5). Data were shown as mean ± SD. Statistical analysis was carried out via a One-way ANOVA test. * refers to $p < 0.05$, ** refers to $p < 0.01$, *** refers to $p < 0.001$, **** refers to $p < 0.0001$, ns refers to no significance.

Supporting Information

Supporting Information is available from the Wiley Online Library or from the author.

Acknowledgements

This work was funded by the National Natural Science Foundation of China (22374071), the National Key R&D Program of China (2021YFF1200700 and 2019YFA0709200), Jiangsu Provincial Key R&D Program (BE2022836), the PAPD Program, State Key Laboratory of Analytical Chemistry for Life Science (5431ZZXM2306), NMPA Key Laboratory for Biomedical Optics (20240001), and Fundamental Research Funds for the Central Universities (202200325, 021314380228, and 021314380195).

Conflict of Interest

The authors declare no conflict of interest.

Data Availability Statement

The data that support the findings of this study are available from the corresponding author upon reasonable request.

Keywords

nanozyme, oxygen-generating, photodynamic therapy, tumor management, Zn^{2+}-overloading therapy

Received: May 1, 2024
Revised: June 25, 2024
Published online:

[1] a) X. Li, J. F. Lovell, J. Yoon, X. Chen, *Nat. Rev. Clin. Oncol.* **2020**, *17*, 657; b) C. He, X. Duan, N. Guo, C. Chan, C. Poon, R. R. Weichselbaum, W. Lin, *Nat. Commun.* **2016**, *7*, 12499; c) D. E. J. G. J. Dolmans, D. Fukumura, R. K. Jain, *Nat. Rev. Cancer* **2003**, *3*, 380.
[2] Z. Shen, Q. Ma, X. Zhou, G. Zhang, G. Hao, Y. Sun, J. Cao, *NPG Asia Mater.* **2021**, *13*, 39.
[3] L. Jiang, H. Bai, L. Liu, F. Lv, X. Ren, S. Wang, *Angew. Chem., Int. Ed.* **2019**, *58*, 10660.
[4] X. Liang, M. Chen, P. Bhattarai, S. Hameed, Z. Dai, *ACS Nano* **2020**, *14*, 13569.
[5] G. Yang, L. Xu, Y. Chao, J. Xu, X. Sun, Y. Wu, R. Peng, Z. Liu, *Nat. Commun.* **2017**, *8*, 902.
[6] C.-P. Liu, T.-H. Wu, C.-Y. Liu, K.-C. Chen, Y.-X. Chen, G.-S. Chen, S.-Y. Lin, *Small* **2017**, *13*, 1700278.
[7] a) S.-Y. Li, H. Cheng, B.-R. Xie, W.-X. Qiu, J.-Y. Zeng, C.-X. Li, S.-S. Wan, L. Zhang, W.-L. Liu, X.-Z. Zhang, *ACS Nano* **2017**, *11*, 7006; b) X. Yang, Y. Yang, F. Gao, J.-J. Wei, C.-G. Qian, M.-J. Sun, *Nano Lett.* **2019**, *19*, 4334; c) Y.-H. Zhang, W.-X. Qiu, M. Zhang, L. Zhang, X.-Z. Zhang, *ACS Appl. Mater. Interfaces* **2018**, *10*, 15030.
[8] C. Wang, J. Yang, C. Dong, S. Shi, *Adv. Therap.* **2020**, *3*, 2000110.
[9] Y. Zhong, Z. Qiu, Y. Li, J. Huang, Z. Lu, R. Kong, N. Yan, H. Cheng, *Chin. Chem. Lett.* **2024**, 109846.
[10] L. Dai, M. Yao, Z. Fu, X. Li, X. Zheng, S. Meng, Z. Yuan, K. Cai, H. Yang, Y. Zhao, *Nat. Commun.* **2022**, *13*, 2688.
[11] S. Zhang, Y. Zhang, Y. Feng, J. Wu, Y. Hu, L. Lin, C. Xu, J. Chen, Z. Tang, H. Tian, X. Chen, *Adv. Mater.* **2022**, *34*, 2206851.
[12] S. Lei, J. Zhang, N. T. Blum, M. Li, D.-Y. Zhang, W. Yin, F. Zhao, J. Lin, P. Huang, *Nat. Commun.* **2022**, *13*, 1298.
[13] a) Y. Huang, G. Qin, T. Cui, C. Zhao, J. Ren, X. Qu, *Nat. Commun.* **2023**, *14*, 4647; b) J. Zhuang, C. Kuo, L. Chou, D. Liu, E. Weerapana, C. Tsung, *ACS Nano* **2014**, *8*, 2812; c) X. Guo, P. Tu, X. Wang, C. Du, W. Jiang, X. Qiu, J. Wang, L. Chen, Y. Chen, J. Ren, *Adv. Mater.* **2024**, *36*, 2313029; d) K. Wei, M. He, J. Zhang, C. Zhao, C. Nie, T. Zhang, Y. Liu, T. Chen, J. Jiang, X. Chu, *Angew. Chem., Int. Ed.* **2023**, *62*, 202307025; e) F. Wu, Y. Li, Y. Meng, X. Cai, J. Shi, J. Li, Y. Chen, L. Zhang, X. Meng, H. Li, X. Jiang, Z. Fu, Y. Wu, W. Bu, *Angew. Chem., Int. Ed.* **2022**, *61*, 202210487; f) Q. Wang, Y. Yu, Y. Chang, X. Xu, M. Wu, G. R. Ediriweera, H. Peng, X. Zhen, X. Jiang, D. J. Searles, C. Fu, A. K. Whittaker, *ACS Nano* **2023**, *17*, 8483.
[14] T. Kambe, T. Tsuji, A. Hashimoto, N. Itsumura, *Physiol. Rev.* **2015**, *95*, 749.
[15] R. G. Uzzo, P. L. Crispen, K. Golovine, P. Makhov, E. M. Horwitz, V. M. Kolenko, *Carcinogenesis* **2006**, *27*, 1980.
[16] M. Murakami, T. Hirano, *Cancer Sci.* **2008**, *99*, 1515.
[17] S. Wu, K. Zhang, Y. Liang, Y. Wei, J. An, Y. Wang, J. Yang, H. Zhang, Z. Zhang, J. Liu, J. Shi, *Adv. Sci.* **2022**, *9*, 2103534.
[18] a) S. S. Sabharwal, P. T. Schumacker, *Nat. Rev. Cancer* **2014**, *14*, 709; b) D. Cen, Q. Ge, C. Xie, Q. Zheng, J. Guo, Y. Zhang, Y. Wang, X. Li, Z. Gu, X. Cai, *Adv. Mater.* **2021**, *33*, 2104037.
[19] B. Ding, H. Chen, J. Tan, Q. Meng, P. Zheng, P. A. Ma, J. Lin, *Angew. Chem., Int. Ed.* **2023**, *62*, 202215307.
[20] M. Du, Z. J. Chen, *Science* **2018**, *361*, 704.
[21] C. Lv, W. Kang, S. Liu, P. Yang, Y. Nishina, S. Ge, A. Bianco, B. Ma, *ACS Nano* **2022**, *16*, 11428.
[22] N. Wiesmann, W. Tremel, J. Brieger, *J. Mater. Chem. B* **2020**, *8*, 4973.
[23] a) A. P. Castano, P. Mroz, M. R. Hamblin, *Nat. Rev. Cancer* **2006**, *6*, 535; b) Z. Yu, P. Zhou, W. Pan, N. Li, B. Tang, *Nat. Commun.* **2018**, *9*, 5044.
[24] a) K. Liang, R. Ricco, C. M. Doherty, M. J. Styles, S. Bell, N. Kirby, S. Mudie, D. Haylock, A. J. Hill, C. J. Doonan, P. Falcaro, *Nat. Commun.* **2015**, *6*, 7240; b) T.-T. Chen, J.-T. Yi, Y.-Y. Zhao, X. Chu, *J. Am. Chem. Soc.* **2018**, *140*, 9912; c) G. Chen, S. Huang, X. Kou, F. Zhu, G. Ouyang, *Angew. Chem., Int. Ed.* **2020**, *59*, 13947.
[25] G. Cheng, W. Li, L. Ha, X. Han, S. Hao, Y. Wan, Z. Wang, F. Dong, X. Zou, Y. Mao, S. Zheng, *J. Am. Chem. Soc.* **2018**, *140*, 7282.
[26] C. Andreini, I. Bertini, A. Rosato, *Acc. Chem. Res.* **2009**, *42*, 1471.
[27] M. T. Lotze, K. J. Tracey, *Nat. Rev. Immunol.* **2005**, *5*, 331.
[28] J. Fucikova, R. Spisek, G. Kroemer, L. Galluzzi, *Cell Res.* **2021**, *31*, 5.
[29] Y. Lee, J. Shinn, C. Xu, H. E. Dobson, N. Neamati, J. J. Moon, *Nat. Commun.* **2023**, *14*, 4771.
[30] Y. Wang, W. Chen, Z. Wang, Y. Zhu, H. Zhao, K. Wu, J. Wu, W. Zhang, Q. Zhang, H. Guo, H. Ju, Y. Liu, *Angew. Chem., Int. Ed.* **2023**, *62*, 202212866.
[31] J. Liu, D. He, T. Hao, Y. Hu, Y. Zhao, Z. Li, C. Liu, D. Chen, Q. Wang, X. Xin, Y. Shen, *Chin. Chem. Lett.* **2024**, *35*, 109296.
[32] H. Lei, Z. Pei, C. Jiang, L. Cheng, *Exploration* **2023**, *3*, 20220001.
[33] H. Peng, F. Yao, J. Zhao, W. Zhang, L. Chen, X. Wang, P. Yang, J. Tang, Y. Chi, *Exploration* **2023**, *3*, 20220115.
[34] P. Liu, X. Xie, M. Liu, S. Hu, J. Ding, W. Zhou, *Acta Pharm. Sin. B* **2021**, *11*, 823.